JOURNAL OF CHEMICAL INFORMATION AND MODELING

Article

pubs.acs.org/jcim

Antiviral Atropisomers: Conformational Energy Surfaces by NMR for Host-Directed Myxovirus Blockers

Craig Grimmer,[†] Terry W. Moore,[§] Aaron Padwa,[‡] Andrew Prussia,[§] Gordon Wells,[∥] Shaoxiong Wu,[‡] Aiming Sun,[§] and James P. Snyder*[,‡,§]

[†]School of Chemistry and Physics, University of KwaZulu-Natal, Pietermaritzburg, South Africa

[‡]Department of Chemistry, Emory University, Atlanta, Georgia 30322, United States

[§]Emory Institute for Drug Development, Emory University, Atlanta, Georgia 30322, United States

[∥]Department of Biochemistry, Stellenbosch University, Stellenbosch, South Africa

Supporting Information

ABSTRACT: Biologically active organic molecules characterized by a high single bond torsional barrier generate isolable isomers (atropisomers) and offer a unique stereochemical component to the design of selective therapeutic agents. The present work presents a nanomolar active inhibitor of myxoviruses, which most likely acts by blocking one or more cellular host proteins but also, serendipitously, exhibits axial chirality with an energy barrier of $\Delta G^{\ddagger} \geq 30$ kcal/mol. The latter has been probed by variable temperature NMR and microwave irradiation and by high level DFT transition state analysis and force field calculations. Full conformational profiles of the corresponding (*aR,S*) and (*aS,S*) atropisomers at ambient temperature were derived by conformer deconvolution with NAMFIS (NMR Analysis by Molecular Flexibility In Solution) methodology to generate seven and eight individual conformations, each assigned a % population. An accurate evaluation of a key torsion angle at the center of the molecules associated with a $^{3}J_{C-S-C-H}$ coupling constant was obtained by mapping the S−C bond rotation with the MPW1PW91/6-31G-d,p DFT method followed by fitting the resulting dihedral angles and *J*-values to a Karplus expression. Accordingly, we have developed a complete conformational profile of diastereomeric atropisomers consistent with both high and low rotational barriers. We expect this assessment to assist the rationalization of the selectivity of the two (*aR,S*) and (*aS,S*) forms against host proteins, while offering insights into their divergent toxicity behavior.

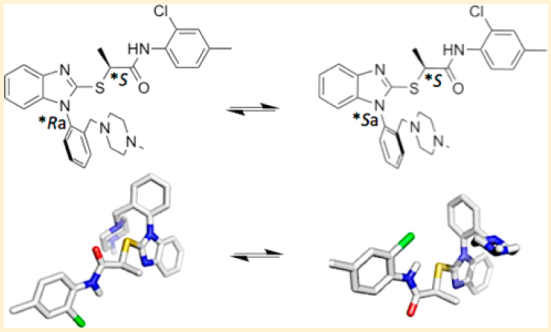

INTRODUCTION

A universal characteristic of antiviral agents directed at viral proteins is their propensity to succumb to resistance as a result of the rapid replication of the target microorganisms in the presence of a selective pressure. This can be overcome by clinical delivery of drug cocktails[1,2] in the context of highly active antiretroviral therapy (HAART).[3] However, an alternative to direct blocking of the action of viral macromolecules is temporary elimination of cellular host factors that support the intracellular reproduction of the microbe. Because viruses of similar genetic origin are likely to employ a similar or common subset of host proteins, antiviral drugs devised in the context of this strategy have the potential to operate as broadly active therapeutic agents. The National Institute of Allergy and Infectious Diseases (NIAID) has strongly encouraged exploration of this approach.[4]

Our laboratories recently complemented several antiviral initiatives directed at viral proteins[5−7] with a high-throughput screening exercise designed to identify small-molecule inhibitors of cellular host proteins employed by myxoviruses.[8] JMN3-003 (**1**) (Scheme 1), a first-generation benzimidazole lead, proved to have 10−70 nM antiviral action against several influenza strains, including respiratory syncytial virus (RSV),

Scheme 1. Small-Molecule Inhibitors of Cellular Host Proteins Employed by Myxoviruses

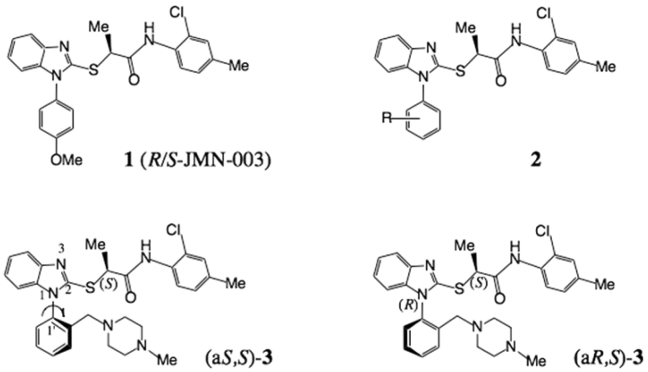

Received: April 2, 2014
Published: July 24, 2014

 © 2014 American Chemical Society

mumps virus (MuV), human para-influenza virus (HPIV3), and measles virus (MeV (Alaska)).[9,10] Due to poor aqueous solubility, the JMN3-003 class was expanded via asymmetric synthesis to series **2** (Scheme 1) with additional hydrophilic functionality and was demonstrated to show improved solubility and potency with superior activity residing in the (*S*)-enantiomers. For example, the piperazine isomers (*aS,S*)-**3** and (*aR,S*)-**3** (Scheme 1) tested against the measles and influenza A viruses were effective at EC_{50} = 68 and 4 nM, respectively. The piperazines not only demonstrated improved potency but also somewhat increased solubility (20 μg/mL) compared to **1** (solubility <15 μg/mL). Morpholino replacements of the piperazine moiety proved to be more soluble still but with reduced potency.[11]

Of interest for its biological significance, analog **3** (Scheme 1) proved to experience atropisomerism[12−14] resulting from restricted rotation about the imidazole-carbon bond (N_1−C_1'). Chemical synthesis afforded each of the (*S*) and (*R*) enantiomers as mixtures of the (*aR,S*)/(*aS,S*) and (*aS,R*)/(*aR,R*) diastereomers. The latter have been isolated by reverse-phase HPLC and have been recrystallized to provide highly enriched crystals of each diastereomer characterized by axial chirality, with stability at room temperature and nanomolar activity against influenza and RSV viruses (EC_{50} = 1−30 nM). However, a given isomer such as (*aR,S*), for example, can be racemized to a 50:50 mixture of (*aR,S*)/(*aS,S*) in MeCN/H_2O in a sealed tube at 100−120° overnight. The torsional interconversion barrier has been estimated to fall between 29 and 30 kcal/mol by both quantum chemical and molecular mechanics methodology.

The conformational complexity of the atropisomers of **3** is not limited to rotation about the N_1−C_1' bond. Once trapped in a deep torsional energy well, each isomer is characterized by its unique conformational profile associated with other easily rotated single bonds. Unraveling this torsional energy surface can provide keys to the binding modes of individual atropisomers to target proteins. In another context, we have shown that the X-ray structures of both protein-bound and free ligands for Hsp90 are members of the corresponding solution ensemble of conformations.[15] With the latter in hand, it becomes possible to deduce binding poses based on experiments in contrast to theoretical docking alone. This approach has been used to resolve the binding pose of Taxol on tubulin,[16] to propose an SAR-compatible binding mode for dictyostatin on the same protein,[17] and to explain the lack of conformational diversity for discodermolide both inside and outside its tubulin binding site.[18] In the present context, we expect that the host factor macromolecule responsible for the actions of **3** diasteroisomers will be identified in subsequent investigations. In anticipation of constructing an empirically based complex between protein and ligand suitable for ligand refinement, we seek to generate a solution ensemble of conformations for each atropisomer. The present work focuses on the more active diastereomers (*aR,S*) and (*aS,S*).

■ METHODS

Synthesis. The compounds employed for the NMR and NAMFIS (NMR Analysis by Molecular Flexibility In Solution; see below) analyses, (*aR,S*)-**3**[19] and (*aS,S*)-**3**, were synthesized as previously described.[11] The *S*-enantiomer of **3**, prepared as a 50:50 mixture of diastereomers, was recrystallized twice from a solution of dichloromethane and ether (90:10) to deliver clear, colorless, orthorhombic crystals greatly enriched in one diastereomer, (*aS,S*)-**3** (99:1, HPLC). The mother liquor was enriched in the (*aR,S*) atropisomer. Each was >95% pure by LC-MS.

^{1}H and ^{13}C NMR Experiments (1-D and 2-D). Experiments were performed at the Department of Chemistry, Emory University (Atlanta, GA, U.S.A.) on a Varian Unity Inova 400 equipped with a 5 mm 4NUC probe operating at 400 MHz (^{1}H) and 100 MHz (^{13}C) and a Varian Unity Inova 600 equipped with either a 5 mm TRES-ZPFG (^{1}H/^{13}C/^{15}N) probe or a 5 mm ID-ZPFG (^{1}H/X) probe operating at 600 MHz (^{1}H) and 150 MHz (^{13}C). Both spectrometers use VNMR 6.1C software. All experiments were conducted with temperature regulation at ∼25 °C. Standard VNMR pulse sequences were used for ^{1}H (s2pul), ^{13}C, APT, COSY (relayh), HETCOR, and NOESY experiments. Long-range ^{1}H−^{13}C correlations were determined using the GHMQC_DA pulse sequence obtained from the Varian applications laboratory in Darmstadt, Germany, and the SELEXCIT and EXSIDE[20,21] pulse sequences obtained from the Varian user library. Data from standard experiments were processed with SpinWorks-3,[22] and data from EXSIDE experiments were processed with VNMR 6.1C. For each probe, ^{1}H pw90 @ tpwr values were measured for each analyte sample. ^{13}C pw90 @ tpwr calibrations were conducted with 30% menthol in $CDCl_3$, and ^{13}C pwx90 @ pwxlvl calibrations were conducted with 1% iodomethane-^{13}C, 1% trimethylphosphite, and 0.2% $Cr(acac)_3$ in $CDCl_3$ (indirect detection test sample).

Samples for quantitative NOESY experiments were prepared by dissolving ∼8 mg of analyte in ∼600 μL of $CDCl_3$ (Cambridge Isotope Laboratories) and were subsequently degassed and sealed. NOESY experiments were performed with mixing times selected in the range of 100−300 ms, and internuclear distances were calculated from cross-peak volumes of the 200 ms data using an internal calibration distance of 2.48 Å for the HCCH fragment of the tolyl ring. The relaxation delay (d1) was 8 s, ∼1.3 × longest T1 of ∼6 s, nt =16, and ni = 256, resulting in an experiment time of ∼20 h.

EXSIDE samples to measure $^3J_{^{13}C-S-C-^1H}$ were prepared by dissolving ∼45 mg of analyte in ∼600 μL of $CDCl_3$ (Cambridge Isotope Laboratories). Shaped pulses for selective excitation (180 g3) were created using Pandora's Box (Pbox) within VNMR 6.1C and tested with the SELEXCIT experiment. The relaxation delay (d1) was 1.5 s, ∼1.3 × T1 of the selectively excited signal of ∼1.2 s, nt = 16, ni = 128, jscale = 30, and jnxh = 6, resulting in an experiment time of ∼3 h (although signals were visible among the noise at ∼30 min). Multiple experiments were performed with narrow ^{13}C sweep widths (∼40 ppm), exploring only those spectral regions with likely ^2J and ^3J coupling to the selectively excited signal (CH at ∼4.9 ppm for both (*aR,S*) and (*aS,S*)).

^{15}N NMR Experiments (2-D). ^{15}N NMR experiments (2-D) were performed at the School of Chemistry and Physics, University of KwaZulu-Natal (Pietermaritzburg, South Africa) on a Bruker Avance III 500 spectrometer equipped with a 5 mm TXI-ZPFG (^{1}H/^{31}P/X) probe operating at 500 MHz (^{1}H) and 51 MHz (^{15}N) with Topspin 2.1pl6 acquisition software. All experiments were performed with temperature regulation at 30 °C. Long-range multiple bond ^{1}H−^{15}N correlations were determined using the HMBCGPLPNDQF pulse program and short-range single bond ^{1}H−^{15}N correlations were determined using the HSQCETGP pulse program. All data were processed with Topspin 2.1pl6. ^{1}H p1 @ pl1 values were measured for each analyte sample; ^{15}N p3 @ pl2 calibrations were conducted with 2% ^{15}N-benzamide in DMSO-d_6.

Samples for ^{1}H-{^{15}N} HMBC/HSQC experiments were prepared by dissolving ∼45 mg of analyte in ∼600 mL of $CDCl_3$ (Cambridge Isotope Laboratories), which were then degassed and sealed (the same samples as used in the EXSIDE experiments). For the HMBC experiments, the relaxation delay (d1) was 1.5 s, ns = 128, td = 4096, td1 = 256, sw1 = 500, o2p = 240, cnst2 = 90, and cnst13 = 8, resulting in an experiment time of ∼18 h. For the HSQC experiments, the relaxation delay (d1) was 2.5 s, ns = 4, td = 1024, td1 = 256, sw1 = 200, o2p = 100, and cnst2 = 90, resulting in an experiment time of ∼50 min.

Karplus Curves for Converting $^{3}J_{C-S-C-H}$ to $\phi_{C-S-C-H}$. Two Karplus[23,24] relationships for the rotation around the S−C bond in C−S−C−H have been described. The first, by Tafazzoli and Giasi[25] (Tafa) is described by eq 1, while the second by Tvaroska et al.[26] (Tvar) is governed by eq 2.

$$^{3}J_{C-S-C-H} = 5.04 \cos 2\varphi - 1.35 \cos \varphi + 0.55 \quad (1)$$

$$^{3}J_{C-S-C-H} = 4.44 \cos 2\varphi - 1.06 \cos \varphi + 0.45 \quad (2)$$

A plot of the two expressions (Figure 1) illustrates that they both describe the torsional landscape in a very similar manner.

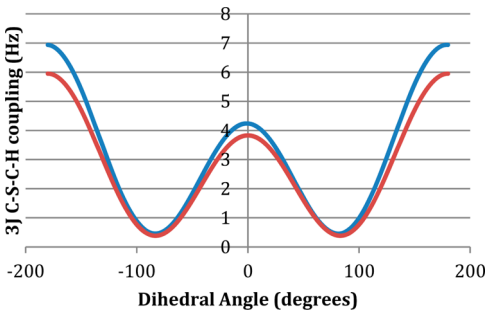

Figure 1. Dependence of $^{3}J_{C-S-C-H}$, Hz, on the dihedral angle $\phi_{C-S-C-H}$, deg, for the Karplus relationships designated Tafa-*J* (blue) and Tvar-*J* (red).

Conformational Analysis. Separate conformer searches for each of the two diastereomers (*aR,S* and *aS,S*) were performed using Schrodinger's Macromodel[27] software with force fields MM3*, MMFF (Merck molecular force field), and OPLS-2005 (optimized potential for liquid simulations) with full-matrix Newton−Raphson (FMNR) minimization within an energy window of 34 kJ/mol (8 kcal/mol) using the generalized Born/surface area (GB/SA) constant dielectric model for the solvent (chloroform). These energy-minimized conformers were combined, and the duplicates were removed within an energy window of 21 kJ/mol (5 kcal/mol).

NAMFIS Conformer Deconvolution. NAMFIS[28,29] is a computational method (NAMFIS (2.5.0) implemented via a series of Python[30] scripts on a 64-bit CentOS[31] (5.8) Linux platform) that intersects a carefully measured NOESY or ROESY NMR spectrum with an optimized set of force field conformations to deconvolute the average NMR spectra of small flexible molecules into individual contributing conformations associated with mole fractions (% populations). Thus, we generate a complete or near-complete set of conformations for a given molecule and intersect the data set with the thermally averaged NOE distances and flexible torsion angles (from $^{3}J_{H-H}$ and $^{3}J_{H-C}$) for the same molecule by a nonleast-squares-fit procedure.[15] The "best-fit" set of conformers each associated with a % population is judged for fitness by a sum of square distances (SSD) metric. A number of NAMFIS alternatives are available,[32,33] but the fundamental basis of the approach, molecular constraints determined using NOE/ROE distances and *J*-torsion angles, is the same.

RESULTS

X-ray Crystal Structure of (*aS,S*)-3. Single crystal X-ray structure analysis of the crystals formed from an ether/dichloromethane mixture showed this atropisomer to be (*aS,S*)-**3** (see Supporting Information for details and a 3D- structure of the compound).

Torsional Barrier Arising from Atropisomerism. (*S*)-**3** presents as a 1:1 mixture of atropisomers in the ^{1}H NMR (DMSO-d_6, 400 MHz) at room temperature as exemplified by the doubled amide NH protons at 10.2−10.3 ppm, a phenomenon absent for the corresponding nonatropisomeric *meta* and *para* piperazine isomers (Supporting Information). Raising the temperature to 120 °C causes only partial coalescence of the doublet. To examine this point further, the (*S*)-**3** diastereomer (99:1 HPLC) in toluene was heated in a sealed tube at 130 °C for 2 h under microwave irradiation conditions resulting in a 98:2 ratio of the two diastereomers (HPLC). At 15 h, the ratio drops to 60:40. The equilibration is clearly solvent dependent[34,35] because 2 h at 130 °C in 75% aq MeCN delivers a diastereomeric ratio of 47:53 (HPLC).

In order to derive an estimate of the rotational barrier resulting from atropisomerism of (*S*)-**3**, we performed quantum chemical and molecular mechanics calculations for rotation about the (imidazole)N_1−C_1'(phenyl) bond for a model system and (*S*)-**3**, respectively. The model system depicted in Figure 2 was treated by performing a quadratic synchronous transition state search (QST3) with the density functional-coupled cluster hybrid M06-2X/cc-pVTZ(-f) to deliver a barrier at 31.4 kcal/mol and a single negative eigenvalue of −69.1 cm^{-1}. The transition structure was confirmed by supplementary

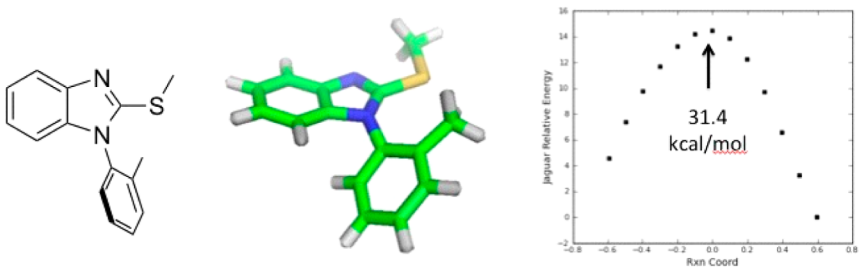

Figure 2. Model for the N−C torsional transition state of (*aS,S*)-**3** with the M06-2X/cc-pVT(-f) density functional using coupled cluster theory resulted in a single negative eigenvalue (−69.1 cm^{-1}) for the transition state at $\Delta E^{\ddagger}$ = 31.4 kcal/mol.

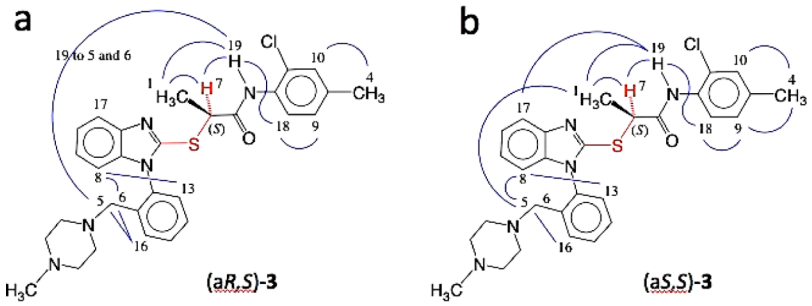

Figure 3. Thirteen and 12 ^{1}H−^{1}H NOE-derived distance constraints (blue lines) for (a) (*aR,S*) and (b) (*aS,S*), respectively. The central $\phi_{C-S-C-H}$ torsional constraint is indicated in red.

intrinsic reaction coordinate (IRC)[36] calculations. The corresponding transition states for *meta* and *para* methyl substitution are 11.3 and 11.0 kcal/mol, respectively. Molecular mechanics evaluation of the rotational transition state for (*aS,S*)-**3** with the OPLS2005/GABA/H_2O protocol provided a barrier of 29.3 kcal/mol. The alternative *meta* and *para* transition state structures fell at 17.1 and 19.4 kcal/mol (for details, see the Supporting Information). Clearly the energy requirements for torsional isomerization of the *ortho*-substituted isomers fall in the range for atropisomers with strongly delayed interconversion.[13]

Chemical Shifts, *J*-Values, and NOE Cross-Peak Assignments. In order to identify the ensembles of equilibrating conformations for both (*aR,S*) and (*aS,S*), we employed a series of 1-D and 2-D NMR experiments (^{1}H, ^{13}C, APT, COSY (relayh), HETCOR, and HMBC/HSQC) for atomic assignment of all ^{1}H, ^{13}C, and ^{15}N atoms in the two diastereomers. The detailed data are presented in the Supporting Information.

^{1}H−^{15}N HSQC and HMBC Correlations. The ^{1}H−^{15}N HSQC experiments reveal the chemical shifts of the amido-^{15}N at 128 ppm for (*aR,S*) and at 127 ppm for (*aS,S*). The HMBC experiments reveal three additional chemical shifts at 37, 157, and 232 ppm for both (*aR,S*) and (*aS,S*). Assignment of the chemical shifts to the nitrogen atoms of the piperazine, amido, and benzimidazole fragments is consistent with observed chemical shifts for ^{15}N in these environments.[37]

There are a number of long-range correlations in the HMBC spectra. Most fall within the "normal" range of 2- to 4-bond H-X contacts typically observed in this type of experiment. While there are no ^2J contacts in the diastereomers, there are two very long-range correlations in both isomers—the first over a distance of 5 bonds (1.62 ppm [^{1}H] to 157 ppm [^{15}N], shifts coincidentally the same for the two compounds) and the second over a distance of 6 bonds (10.51 ppm [^{1}H] to 232 ppm [^{15}N] and 10.41 ppm [^{1}H] to 232 ppm [^{15}N]). Although unusual, several literature precedents for correlations over similar distances have been reported: ^5J between ^{1}H and ^{31}P,[38] ^6J between ^{1}H and ^{183}W,[39] ^6J between ^{1}H and ^{117}Sn,[40,41] and ^7J between ^{1}H and ^{31}P,[42] using HMBC-style experiments. Graphical illustrations are located in the Supporting Information.

NOESY and Generation of Averaged 1H---1H Distances for (*aR,S*) and (*aS,S*). Internuclear distances were obtained by the established method[43−51] of calculating cross-peak volumes (τ_m = 200 ms) based on the isolated spin pair approximation (ISPA)[52] using an internal calibration distance of 2.48 Å for the HCCH fragment of the tolyl ring. The (*aR,S*) and (*aS,S*) atropisomers delivered 13 and 12 cross-peaks, (2.3−3.5 Å), respectively, including the 2.48 Å internal standard. Figure 3 graphs the through-space cross-peak interactions for the two isomers. Numerical details are found in the Supporting Information.

Prediction of *J*-Dependent C−S−C−H Dihedral Angles by DFT. Given that the Tafa and Tvar Karplus curves were derived from thioglycoside and aldohexopyranoside structures, we sought an independent measure of the dihedral angle predictions for $^3J_{C-S-C-H}$. A DFT density functional theory (DFT) *J*-coupling curve was generated for a truncated structure of *S*-chirality at the central methylated carbon by freezing $\phi_{C-S-C-H}$ at the 25 dihedral angles indicated in Figure 4 followed

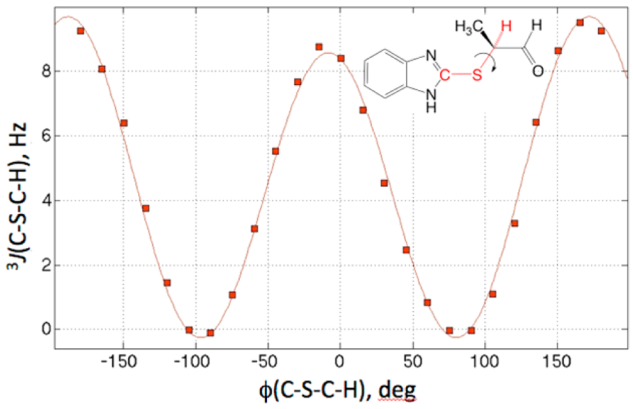

Figure 4. DFT generated Karplus curve for the C−S−C−H dihedral angle (15° increments) in a truncated structure at the core of the linker region in (*aR,S*)-**3** and (*aS,S*)-**3**.

by geometry optimization of all other internal variables (DFT: MPW1PW91[53,54]/6-31G-d,p). Coupling constant calculations were performed with GIAO[55,56] (gauge including atomic orbitals) for the constraint-optimized structures with the same method and basis set. Rotation of the C−S−C−H angle in both directions delivers the same result (Supporting Information). All DFT calculations were performed within the Gaussian09 series of programs.[57] The EXSIDE coupling constants of 5.0 and 4.7 Hz (see below) predict $\phi_{C-S-C-H}$ as shown in Table 1.

The *J*-values plotted in Figure 4 were fitted with a nonlinear regression model using MatLab.[58] Unlike the Tafa and Tvar curves symmetrical about ϕ = 0° (Figure 1), the DFT plot is shifted 8.2° to the left. The resulting Karplus equation (root mean squared error = 0.28; r^2 = 0.994; *p*-value = 9.03e-24) follows

$$^3J_{C-S-C-H} = 9.38 \cos 2(\varphi + 8.20) - 0.56 \cos(\varphi + 8.20) - 0.25 \quad (3)$$

Atropisomer Three-Bond Coupling Constants and Corresponding Dihedral Angles. Two coupling constants

Table 1. $J_{C_q-S-C-H}$ Values for (*aR,S*)-3 and (*aS,S*)-3 Derived from EXSIDE Analysis

	(*aR,S*)	(*aS,S*)
$^3J_{Cq-S-C-H}$ from EXSIDE experiment, Hz	5.0	4.7
C_q−S−C−H dihedral angles (Tafa), deg	±144.7/±215.4	±141.6/±218.4
C_q−S−C−H dihedral angles (Tvar), deg	±154.2	±150.0
C_q−S−C−H dihedral angles (DFT), deg	127.6/30.8/−47.2/−144.0	125.7/33.0/−49.4/−142.1

each were determined for the central linker between the benzimidazole and the amide. $^3J_{HH}(CH_3-CH)$ at the stereogenic carbon is conformationally uninformative, delivering, as expected, the same value for both isomers (7.3−7.4 Hz). In order to derive torsional information within the molecular fulcrum, we measured the $^3J_{CH}(C_q-S-C-H)$ values for each atropisomer with the EXSIDE pulse sequence to be 5.0 and 4.7 Hz, respectively (see Supporting Information for a comparison of Karplus curves). The spectrum for (*aR,S*) is shown in Figure 5.

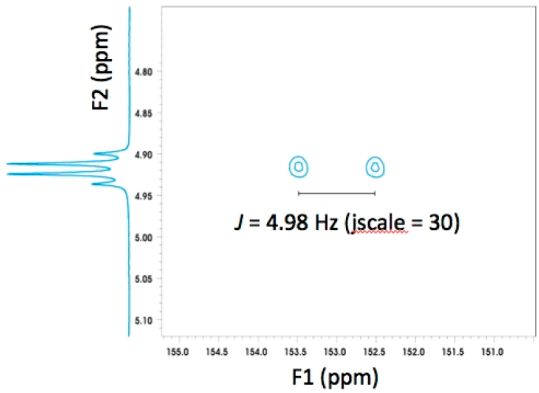

Figure 5. EXSIDE spectrum for (*aR,S*): $^3J_{CH}(C_q-S-C-H)$ = 4.98 Hz. The $^3J_{HH}(CH_3-CH)$ value for H7 at the stereogenic center is presented as a quartet to the left.

The corresponding torsion angles from the Tafa and Tvar Karplus expressions (eqs 1 and 2) are presented in Table 1.

If the coupling constant results were reflective of a single conformation for each isomer, then one of the four tabulated angles is expected to represent it. However, because the linker that contains the C−S−C−H torsion is engaged in a dynamic equilibrium of several conformations, the results indicate a very similar dihedral angle average for each member of the pair. NAMFIS analysis discussed below provides a resolution of the problem in terms of a distribution of specific conformations. In spite of the similar coupling constant, the solution-based distribution does not deliver conformational families with identical $^3J_{C-H}$ profiles (see below).

Modeled Conformational Pools for (*aR,S*) and (*aS,S*). Separate conformer searches for each of the two diastereomers with eight rotatable bonds were performed using the MM3*, MMFF, and OPLS-2005 force fields in Macromodel[27] supplemented with the $CHCl_3$ GBSA solvent continuum model. With an energy window of 8 kcal/mol, each 10,000 step search led to 1000−3400 conformers (Supporting Information). The combined and duplicate-free energy-minimized conformers with an energy cap of 5 kcal/mol were clustered by means of a specific filter based on the C−C−N−C dihedral angle. This tactic allowed separation of the (*aR,S*) and (*aS,S*) isomers and simultaneously removed high energy conformers with axially substituted piperazine rings. The result was a pool of 53 conformers for (*aR,S*)-isomer and 167 conformers for (*aS,S*). These data sets served as input to the subsequent NAMFIS analysis.

NAMFIS Analyses for (*aR,S*) and (*aS,S*). Table 2 summarizes the outcomes of the NAMFIS analyses for both atropisomers by searching the individual conformer pools of 53 and 167 structures, respectively, for compliance with the NMR NOE-distance and *J*-coupling constraints. With a SSD of 3−5, the data for the (*aR,S*) diastereomer are very well fitted by the nine selected NAMFIS conformations. Irrespective of the applied Karplus equation (Tafa, Tvar, DFT), the top two selections (NAMFIS-1 and -2) are the same, accounting for nearly half of the solution distribution.

At a SSD of 5, the more active (*aS,S*) form is equally well fitted by 10 selected NAMFIS rotamers. Again, the top two selections (NAMFIS-10 and -11), accounting for roughly half the solution distribution, are the same irrespective of the Karplus equation (Tafa, Tvar, DFT).

For the eight conformation (*aR,S*) data set, the conformational distribution ranges from 26% to 1%. It is essentially identical upon application of the Tafa and Tvar Karplus equations, both in the order and magnitude of the mole fractions (presented as % population). The one difference is the elimination of the 1% contribution of NAMFIS-8 in the Tvar context. Using the DFT-derived Karplus equation, the distribution changes somewhat, with the largest difference being the displacement of NAMFIS-4 (14%) by NAMFIS-9 (11%), with smaller changes in the order of selection. The (*aS,S*) isomer delivered the same four conformations as the major part (90%) of the conformer pool the with essentially the same % populations (29−17%) regardless of the C−S−C−H Karplus expression employed (Tafa and Tvar). For the remainder of the population, the order of selection changed and Tvar delivered one extra conformer at 1% contribution level. Using the DFT-based Karplus equation, three additional conformers are selected (NAMFIS-18, -19, and -20), accounting for a total of roughly 26% of the distribution. In all three cases, the top two conformers selected from the pool are the same (NAMFIS-10, -11, and -12), accounting for roughly half the conformer distribution.

■ DISCUSSION

NAMFIS Conformer Distributions for (*aR,S*) and (*aS,S*). The typical NAMFIS approach, parsing an averaged NMR spectrum into individual conformers, relies on geometric constraints imposed by homonuclear NOEs ($^1H-^1H$ distances, Å) and homonuclear three bond coupling constants ($^3J_{H-H}$ to $\phi_{H-C-C-H}$). (There are no such constraints in the central part of (*aR,S*) and (*aS,S*); see below.) In the present cases, the conformational analyses are subject to a dozen NOE-derived distances <3.5 Å involving protons on the monocyclic aromatic rings at the termini of the structures (e.g., H5, H6, and H18) and several torsionally diagnostic connections within the central linker between them (e.g., H1, H7 and H19), Figure 3. Particularly important is the reach of the amide proton H19

Table 2. Features and Results of NAMFIS Analysis for (*aR,S*)-3 and (*aS,S*)-3[a]

	(*aR,S*)	(*aS,S*)
no. candidate conformers	53	167 + 1[b]
no. NOE, *J* constraints	13, 1 ($^3J_{Cq-S-C-H}$)	12, 1 ($^3J_{Cq-S-C-H}$)
no. NAMFIS selected conformers with Tafa	8	7
selected conformers	NAMFIS-1−8	NAMFIS-10−16
conformer no., population, ΔG_{rel}, ϕ(C−S−C−H)	1:26% (0.0)/−40.4°	10:28% (0.0)/+171.3
	2: 17 (0.3)/+24.3	11: 23 (0.1)/+24.5
	3: 14 (0.4)/+52.7	12: 21 (0.2)/+34.3
	4: 14 (0.4)/+45.9	13: 17 (0.3)/−46.2
	5: 12 (0.5)/−13.4	14: 6 (0.9)/+49.5
	6: 10 (0.6)/+47.1	15: 5 (1.0)/+179.8
	7: 6 (0.9)/+51.7	16: 1 (2.0)/+37.4
	8: 1 (1.9)/−175.7	
SSD	4.7	4.1
no. NAMFIS selected conformers with Tvar	7	8
selected conformers	NAMFIS-1−7	NAMFIS-10−17
conformer no, population, ΔG_{rel}, ϕ(C−S−C−H)	1: 27 (0.0)/−40.4	10:30% (0.0)/+171.3
	2: 17 (0.3)/+24.3	11: 23 (0.2)/+24.5
	3: 14 (0.4)/+52.7	12: 22 (0.2)/+34.3
	4: 14 (0.4)/+45.9	13: 17 (0.3)/−46.2
	5: 12 (0.5)/−13.4	15: 4 (1.2)/+179.8
	6: 10 (0.6)/+47.1	14: 3 (1.4)/+49.5
	7: 7 (0.8)/+51.7	16: 1 (2.0)/+37.4
		17: 1 (2.0)/+173.7
SSD	5.0	4.2
no. NAMFIS selected conformers with DFT	7	8
selected conformers	NAMFIS-1, -2, -3, -5, -6, -7, -9	NAMFIS-10, -11, -13, -14, -16, -18, -19, -20
conformer no., population, ΔG_{rel}, ϕ(C−S−C−H)	1: 26 (0.0)/−40.4	10: 28 (0.0)/+171.3
	2: 18 (0.2) /+24.3	11: 25 (0.1)/+24.5
	5: 16 (0.3) /−13.4	18: 18 (0.3)/+62.0
	3: 13 (0.4)/+52.7	14: 11 (0.6)/+49.5
	9: 11 (0.5)/+59.6	13: 9 (0.7)/−46.2
	6: 10 (0.6)/+47.1	19: 4 (1.2)/+60.7
	7: 7 (0.8)/+51.7	20: 4 (1.2)/+170.6
		16: 1 (2.0)/+37.4
SSD	3.4	4.4

[a]Population, %; ΔG_{rel}, kcal/mol; ϕ(C−S−C−H), deg; $^3J_{Cq-S-C-H}$, Hz. [b]X-ray structure.

that correlates both within the linker and to the flanking aromatic rings in (*aR,S*) and (*aS,S*). To add one additional boundary condition to the flexible linker, the ^3J heteronuclear ^{13}C−S−C^1−H coupling constant was also determined. The set of constraints for (*aR,S*) results in an excellent fit to the experimental data by either 7 or 8 conformers (Tvar or Tafa) as monitored either by the diminutive SSD = 5 or by the deviations between the experimental and calculated internuclear distances (Δ_{max} 9%). Apart from the eighth conformer (NAMFIS-8) making a diminutive contribution to the population (∼1%) derived with Tafa, the NAMFIS-selected conformers are independent of the Karplus equation applied (Figure 1, Table 1), both in the order of selection and the proportion of the population. The dominant conformer (NAMFIS-1) accounts for ∼27% of the population. The largest deviation between the experimental and calculated data is found in the $^3J_{C-S-C-H}$ coupling constant (J_{exp} 4.98 Hz vs J_{calc} 2.58 Hz [Tafa], Δ^3J = 2.4 Hz). However, the coupling constant constraint is based upon a Karplus-type relationship for carbohydrate derivatives. A more appropriate relationship accounting for the electronegativity and the orientation of the substituents in *aR,S*-**3** would be expected to deliver a better fit.

The NMR constraints for (*aS,S*) yields a satisfying fit to experiment in its best-fit selection of 8 conformations (SSD = 4). There is no particularly dominant conformer, with NAMFIS-10 at ∼29% and NAMFIS-11 at ∼23%. The averaged coupling constant better matches the NAMFIS deconvolution (J_{exp} 4.65 Hz vs J_{calc} 4.12 Hz [Tafa], Δ^3J = 0.53 Hz) than that for (*aR,S*) with one deviation of >0.5 Å between the experimental and calculated internuclear distances (H17−H19). Again, the application of a ^3J vs φ relationship for carbohydrate derivatives may not be entirely appropriate; Δ^3J = 0.96 Hz for Tvar.

Using the DFT-generated Karplus relationship (DFT) for $^3J_{C-S-C-H}$, NAMFIS analysis selected seven and eight conformers from the conformer pools for the (*aR,S*) and (*aS,S*) isomers, with similar SSD values ((*aR,S*): 3; (*aS,S*): 4)). Significantly, the top two selections are the same as those for Tafa and Tvar for both the (*aR,S*) and (*aS,S*) isomers. For (*aR,S*), one new selection from the pool NAMFIS-9 at the level of 11% displaces NAMFIS-4 from the TAFA and TVAR selections. For (*aS,S*), three new selections from the pool NAMFIS-18, NAMFIS-19, and NAMFIS-20 at the levels of 18%, 4%, and 4%, respectively, displace NAMFIS-12 and NAMFIS-15 from the TAFA and TVAR selections.†

NAMFIS analysis delivers three broad classes of molecular conformations in both the (*aR,S*) and (*aS,S*) data sets: "L" ((*aR,S*)-NAMFIS-1; (*aS,S*)-NAMFIS-13), "U" ((*aR,S*)-NAMFIS-2−7; (*aS,S*)-NAMFIS-10, -14, -15, -17), and "S" ((*aR,S*)-NAMFIS-8; (*aS,S*)-NAMFIS-11, -12, -16). The letter designations are a rough reflection of the overall molecular shape. The U-forms present terminal rings as stacked hydrophobic centers, a type of "syn" organization between the methyl-piperizine chloro-phenyl moieties with respect to the benzimidazole ring. Transformation from U to S results in an approximate "anti" spatial relationship between the same two groups. It is noteworthy that the U-geometry represents the majority population of conformers (∼70%) for (*aR,S*). By contrast, (*aS,S*) is characterized by a more even distribution of the three conformer classes, with the largest represented class, "S", at ∼46% of the population distribution.

One might be tempted to draw the conclusion that the difference in conformer distributions for (*aR,S*) and (*aS,S*) is a determinant for the superior biological activity of the latter atropisomer. However, it should be recalled that the conformer pool associated with each conformational manifold corresponds to a rapidly equilibrating set of torsional isomers, 7 or 8 for both (*aR,S*) and (*aS,S*). Furthermore, a Boltzmann distribution of the populations (Table 2) reveals that all the NAMFIS conformers are within ΔG = 2 kcal/mol of their respective global minima (i.e., NAMFIS-1 and NAMFIS-8, respectively, for (*aR,S*) and NAMFIS-10 and NAMFIS-16, respectively, for (*aS,S*)). Consequently, all three conformer classes are readily accessible to any ligand binding site associated with a viral target for the drug candidates. What does, however, distinguish (*aR,S*) and (*aS,S*) is their diastereomeric relationship. Close examination of the **a** vs **b**, **c** vs **d** and **e** vs **f** pairs in Figure 6

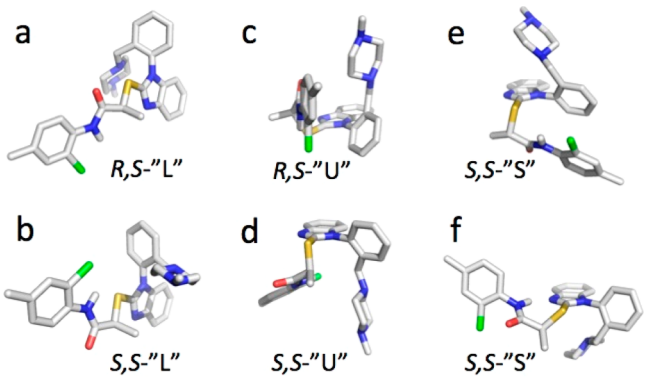

Figure 6. Three NAMFIS conformer classes "L", "U", and "S" represented by examples from the (*aR,S*) and (*aS,S*) diastereomers. Each comparison (a vs b, c vs d, and e vs f) is depicted to show reorganization of the conformation as the N_1-C_1' bond rotates between the (*R*) and (*S*) atopisomers.

highlights that rotation about the N_1-C_1' bond responsible for the axial chirality generates fundamentally different stereochemistries. One of these (i.e., (*aS,S*)) is fully compatible with the presently unknown host protein target in conjunction with one of the three conformational classes.

The X-ray Crystal Structure of (*aS,S*)-3 Is Absent from the NAMFIS Conformations in Solution. It is of interest that the single crystal X-ray crystal structure of (*aS,S*)-**3** is not found among the NAMFIS solution conformers. Adding it explicitly to the pool of 167 candidates (Table 2) prior to NAMFIS fitting leads to the same result. The outcome is further reinforced by fitting the X-ray structure alone to the NMR data leading to the rather high SSD = 77 (output files in Supporting Information). This is surprising in light of previous NAMFIS analyses for diverse molecular structures in which the crystal structure appears as a member of the conformational pool.[15,16,18,59]

The X-ray structure (Figure 7a) illustrates membership in the "S" conformational class. It differs from the dominant

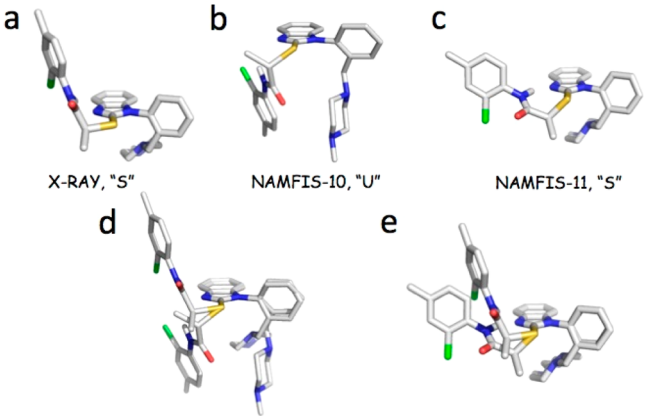

Figure 7. Comparison of conformers of (*aS,S*): (a) X-ray structure of (*aS,S*)-**3**, (b) NAMFIS-10, (*aS,S*)-"U" form, (c) NAMFIS-11, (*aS,S*)-"S" form, (d) superposition of X-ray and NAMFIS-10, and (e) superposition of X-ray and NAMFIS-11.

conformation in the (*aS,S*) pool ((*aS,S*)-NAMFIS-10 (28% population, DFT Karplus), "U"-class, Figure 7b) in primarily one key torsional angle in the central linker region by 144°, namely, ϕ(CSC(Me)C(O)), −85° in the crystal structure and 59° in NAMFIS-10. This torsional variation strongly influences the fitting of NOE-derived distances (Supporting Information) stemming from the critical H1−H7, H5/6−H8, and H1−H5/6 atoms (Figure 3). We presume that the crystal lattice has captured a low energy rotamer that is not a local minimum in $CDCl_3$ solution. The closest match between the X-ray structure ("S"-class) and the NAMFIS selected conformers from the (*aS,S*) pool is NAMFIS-11 (25% population, DFT Karplus), also necessarily of the "S" class. The key torsional angle ϕ(CSC(Me)C(O)) for NAMFIS-11 is −94°, a difference of only 9° from the same angle in the X-ray structure.

Torsion Angle Distributions: Averaged vs NAMFIS. The present EXSIDE measurements have generated 5.0 and 4.7 Hz three-bond coupling constants for the $C_q-S-C-H$ chain of atoms in (*aR,S*)-**3** and (*aS,S*)-**3**, respectively. The Tafa Karplus expression assigns ±145°, ±215° (*aR,S*) and ±142°, ±218° (*aS,S*) to them, while the Tvar expression assigns the corresponding values ±154°, ±206° (*aR,S*) and ±150°, ±210° (*aS,S*) (Table 1). The quantum chemical DFT Karplus curve for a truncated structure (Figure 4) posits −144° and +128° (*aR,S*) and −142° and +126° (*aS,S*), plus two additional angles of −47° and +31° (*aR,S*) and −49° and +33° (*aS,S*) arising from a different shape of the DFT curve vs the Tafa and Tvar curves in the −90° to +90° degree range (Tafa and Tvar offer no solution for the measured coupling constants in this region). The difference between the average ^3J-coupling constant calculated by the NAMFIS analysis and the experimental value indicates an improvement, ΔJ = 0.36 Hz (*aR,S*) and ΔJ = 0.77 Hz (*aS,S*) of the fit using the DFT curve. Although the two

most populated conformers selected by NAMFIS for all three curves are the same, the differences in the other selected conformers and their relative abundance results in an improved SSD for (*aR,S*) but no material improvement for (*aS,S*). The addition of the two extra C_q−S−C−H torsion angles satisfying the experimental *J*-coupling constraint in the DFT-calculated Karplus relationship offers a better match to the majority of angles from the NAMFIS selections, NAMFIS-1 to -7 and -9 for *aR,S* and NAMFIS-11 to -14, -16, -18, and -19 for (*aS,S*) because most of the NAMFIS selections present angles in the −41° to +52° region for (*aR,S*) and in the −47° to +62° region for (*aS,S*). Considering the top two NAMFIS selections for (*aR,S*) and (*aS,S*) (the same, selected by all three Karplus relationships), both of the selections for (*aR,S*), NAMFIS-1 (C−S−C−H = −40.4°) and NAMFIS-2 (C−S−C−H = +24.3°) are reasonably matched by the DFT-Karplus solutions (−47°, +31°), while only the second selection for (*aS,S*), NAMFIS-11 (C−S−C−H = +24.5°) finds a reasonable DFT-Karplus match (+33°). The top selection for (*aS,S*), NAMFIS-10 (C−S−C−H = +171.3°) is not matched.

Within the (*aR,S*) and (*aS,S*) conformational manifolds, all of the rotational isomers are in rapid equilibrium. We regard it as coincidental that the dihedral angles derived from the averaged experimental coupling constants are actually correlated with a similar torsion angle window displayed by the DFT-NAMFIS-selected conformers. There are many other combinations of torsion angles that can also accommodate the experimental data. However, given this single *J*-coupling constraint, this represents the best fit for each of the two diastereomers. Other molecular systems with different atomic constitutions and steric requirements are certain to exhibit such behavior. In summary, any given measured ^3J value obtained from a flexible molecular architecture may well translate into a Karplus-derived torsion that is significantly different from those displayed by members of a corresponding mobile conformational ensemble.

■ CONCLUSIONS

Atropisomer axial chirality is a potentially valuable stereochemical adjunct to the development of selective agents in drug discovery. While such compounds are not plentiful in the clinic, recent reviews describe both applications and challenges in their development.[12,13] The present work describes the discovery that compound **3** not only proves to be an effective inhibitor of myxoviruses, most likely by blockade of one or more host proteins in the nanomolar range,[11] but also, serendipitously, exhibits axial chirality. This observation motivated an attempt to address two questions in parallel. The first is the magnitude of the C−N torsion barrier separating rotomeric diastereomers. Namely, is it high enough to allow development of one atropisomer as a single compound? The question appears to have been answered in the positive ($\Delta G^{\ddagger} \geq 30$ kcal/mol). The second problem concerns the bioactive conformation of **3** in the currently unknown host protein target. We have demonstrated previously that knowledge of solution conformations of a drug molecule can significantly accelerate the determination of the bound conformer for a known target.[15,16,60−62] In the present instance, we have reversed the process and determined the solution conformations of (*aS,S*)-**3** and (*aR,S*)-**3** ahead of discovery of the protein target.

In addition, we have, for the first time, developed a complete conformational profile of diastereomeric atropisomers that is consistent with both high and low rotational barriers (Figure 8). We expect this assessment to assist the rationalization of the selectivity of the two key forms against host proteins while providing insights into divergent toxicity behavior of the atropisomers.

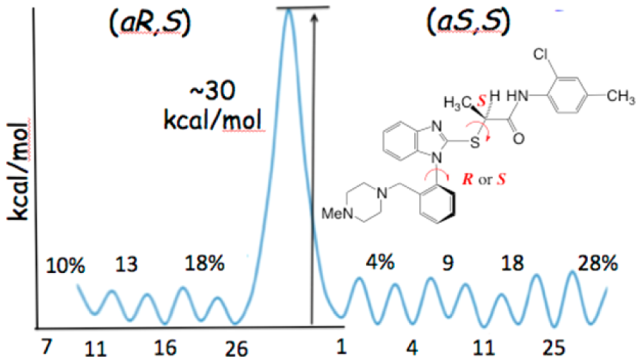

Figure 8. Conformational landscape for (*aR,S*)-**3** and (*aS,S*)-**3**. The two atropisomer conformational pools are separated by a large barrier at ambient temperature. The rapidly averaged low barrier conformers are characterized by % populations indicated on either sides of the ~30 kcal/mol barrier responsible for the axial chirality.

■ ASSOCIATED CONTENT

Supporting Information

NMR assignments for (*aR,S*)-**3** and (*aS,S*)-**3**, details for conformational searching, NAMFIS analysis, comparison of the $^3J_{C-S-C-H}$ Karplus curves, X-ray data, and details concerning the atropisomeric torsion barrier. This material is available free of charge via the Internet at http://pubs.acs.org.

■ AUTHOR INFORMATION

Corresponding Author

*E-mail: jsnyder@emory.edu.

Author Contributions

C.G. and J.P.S. designed the study. C.G., J.P.S., A.P., A.P., and A.S. contributed to writing the paper. C.G., J.P.S., S.W., T.W.M., and A.S. contributed to the editing of the manuscript and interpretation of data.

Notes

The authors declare no competing financial interest.

■ ACKNOWLEDGMENTS

C.G. acknowledges financial assistance from Emory College of Emory University and the National Research Foundation (South Africa) and is grateful to Ron Crouch of Agilent Technologies (Loveland, Colorado) for assistance with the EXSIDE experiments. We are also grateful to Professor Dennis Liotta for support, Dr. John Bacsa for the X-ray structure of (*aS,S*)-**3**, and Drs. Bing Wang, Ana Alcaraz (both Emory University), and Cathryn Slabber (University of Kwazulu-Natal, South Africa) for informative and enlightening discussion.

■ REFERENCES

(1) Sawyers, C. L. Cancer: Mixing cocktails. *Nature* **2007**, *449*, 993−996.

(2) Smith, C. V.; Sharma, V.; Sacchettini, J. C. TB drug discovery: Addressing issues of persistence and resistance. *Tuberculosis* **2004**, *84*, 45−55.

(3) Mills, E. J.; Nachega, J. B.; Bangsberg, D. R.; Singh, S.; Rachlis, B.; Wu, P.; Wilson, K.; Buchan, I.; Gill, C. J.; Cooper, C. Adherence to HAART: A systematic review of developed and developing nation patient-reported barriers and facilitators. *PLoS Med.* **2006**, *3*, e438.

(4) NIAID 2011 Influenza Antiviral Research Pipeline Workshop. National Institute of Allergy and Infectious Diseases (NIAID). http://www.niaid.nih.gov/about/organization/dmid/meetings/Documents/fluantiviralwkshop2011.pdf (accessed July 16, 2014).
(5) Sun, A.; Yoon, J.-J.; Yin, Y.; Prussia, A.; Yang, Y.; Min, J.; Plemper, R. K.; Snyder, J. P. Potent non-nucleoside inhibitors of the measles virus RNA-dependent RNA polymerase complex. *J. Med. Chem.* **2008**, *51*, 3731−3741.
(6) Yoon, J.-J.; Krumm, S. A.; Ndungu, J. M.; Hoffman, V.; Bankamp, B.; Rota, P. A.; Sun, A.; Snyder, J. P.; Plemper, R. K. Target analysis of the experimental measles therapeutic AS-136A. *Antimicrob. Agents Chemother.* **2009**, *53*, 3860−3870.
(7) Ndungu, J. M.; Krumm, S. A.; Yan, D.; Arrendale, R. F.; Reddy, G. P.; Evers, T.; Howard, R.; Natchus, M. G.; Saindane, M. T.; Liotta, D. C.; Plemper, R. K.; Snyder, J. P.; Sun, A. Non-nucleoside inhibitors of the measles virus RNA-dependent RNA polymerase: Synthesis, structure−activity relationships, and pharmacokinetics. *J. Med. Chem.* **2012**, *55*, 4220−4230.
(8) Yoon, J.-J.; Chawla, D.; Paal, T.; Ndungu, M.; Du, Y.; Kurtkaya, S.; Sun, A.; Snyder, J. P.; Plemper, R. K. High-throughput screening-based identification of paramyxovirus inhibitors. *J. Biomol. Screening* **2008**, *13*, 591−608.
(9) Sun, A.; Ndungu, J. M.; Krumm, S. A.; Yoon, J.-J.; Thepchatri, P.; Natchus, M.; Plemper, R. K.; Snyder, J. P. Host-directed inhibitors of myxoviruses: Synthesis and in vitro biochemical evaluation. *ACS Med. Chem. Lett.* **2011**, *2*, 798−803.
(10) Krumm, S. A.; Ndungu, J. M.; Yoon, J. J.; Dochow, M.; Sun, A.; Natchus, M.; Snyder, J. P.; Plemper, R. K. Potent host-directed small-molecule inhibitors of myxovirus RNA-dependent RNA-polymerases. *PLoS One* **2011**, *6*, e20069.
(11) Moore, T. W.; Sana, K.; Yan, D.; Thepchatri, P.; Ndungu, J. M.; Saindane, M. T.; Lockwood, M. A.; Natchus, M. G.; Liotta, D. C.; Plemper, R. K.; Snyder, J. P.; Sun, A. Asymmetric synthesis of host-directed inhibitors of myxoviruses. *Beilstein J. Org. Chem.* **2013**, *9*, 197−203.
(12) Clayden, J.; Moran, W. J.; Edwards, P. J.; LaPlante, S. R. The challenge of atropisomerism in drug discovery. *Angew. Chem., Int. Ed.* **2009**, *48*, 6398−6401.
(13) LaPlante, S. R.; Edwards, P. J.; Fader, L. D.; Jakalian, A.; Hucke, O. Revealing atropisomer axial chirality in drug discovery. *ChemMedChem.* **2011**, *6*, 505−513.
(14) Alkorta, I.; Elguero, J.; Roussel, C.; Vanthuyne, N.; Piras, P. Chapter 1 − Atropisomerism and axial chirality in heteroaromatic compounds. *Adv. Heterocycl. Chem.* **2012**, *105*, 1−188.
(15) Thepchatri, P.; Eliseo, T.; Cicero, D. O.; Myles, D.; Snyder, J. P. Relationship among ligand conformations in solution, in the solid state, and at the Hsp90 binding site: Geldanamycin and radicicol. *J. Am. Chem. Soc.* **2007**, *129*, 3127−3134.
(16) Ganesh, T.; Guza, R. C.; Bane, S.; Ravindra, R.; Shanker, N.; Lakdawala, A. S.; Snyder, J. P.; Kingston, D. G. I. The bioactive taxol conformation on β-tubulin: Experimental evidence from highly active constrained analogs. *Proc. Natl. Acad. Sci. U.S.A.* **2004**, *101*, 10006−10011.
(17) Jogalekar, A. S.; Damodaran, K.; Kriel, F. H.; Jung, W.-H.; Alcaraz, A. A.; Zhong, S.; Curran, D. P.; Snyder, J. P. Dictyostatin flexibility bridges conformations in solution and in the β-tubulin taxane binding site. *J. Am. Chem. Soc.* **2011**, *133*, 2427−2436.
(18) Jogalekar, A. S.; Kriel, F. H.; Shi, Q.; Cornett, B.; Cicero, D.; Snyder, J. P. The discodermolide hairpin structure flows from conformationally stable modular motifs. *J. Med. Chem.* **2009**, *53*, 155−165.
(19) (*aR,S*) = (*R/S*)-EMXV-01492 = (*R/S*)-N-(2-chloro-4-methylphenyl)-2-((1-(2-((4-methylpiperazin-1-yl)methyl)phenyl)-1H-benzo[d]imidazol-2-yl)thio)propanamide.
(20) Krishnamurthy, V. V. Excitation-sculptured indirect-detection experiment (EXSIDE) for long-range CH coupling-constant measurement. *J. Magn. Reson., Ser. A* **1996**, *121*, 33−41.
(21) Butts, C. P.; Heise, B.; Tatolo, G. SelEXSIDE: Fast and easy measurement of multiple-bond $^{1}H,^{13}C$ coupling constants for stereochemical analysis. *Org. Lett.* **2012**, *14*, 3256−3259.
(22) Marat, K. SpinWorks. Nuclear Magnetic Resonance Lab, Department of Chemistry, University of Manitoba. http://home.cc.umanitoba.ca/~wolowiec/spinworks/index.html (accessed July 16, 2014).
(23) Karplus, M. Contact electron spin coupling of nuclear magnetic moments. *J. Chem. Phys.* **1959**, *30*, 11−15.
(24) Karplus, M. Vicinal proton coupling in nuclear magnetic resonance. *J. Am. Chem. Soc.* **1963**, *85*, 2870−2871.
(25) Tafazzoli, M.; Ghiasi, M. New Karplus equations for ^{2}JHH, ^{3}JHH, ^{2}JCH, ^{3}JCH, ^{3}JCOCH, ^{3}JCSCH, and ^{3}JCCCH in some aldohexopyranoside derivatives as determined using NMR spectroscopy and density functional theory calculations. *Carbohydr. Res.* **2007**, *342*, 2086−2096.
(26) Tvaroska, I.; Mazeau, K.; Blanc-Muesser, M.; Lavaitte, S.; Driguez, H.; Taravel, F. R. Karplus-type equation for vicinal carbon-proton coupling constants for the C-S-C-H pathway in 1-thioglycosides. *Carbohydr. Res.* **1992**, *229*, 225−231.
(27) Product Suites, Schrodinger. http://www.schrodinger.com/MacroModel (accessed July 16, 2014).
(28) Cicero, D. O.; Barbato, G.; Bazzo, R. NMR analysis of molecular flexibility in solution: A new method for the study of complex distributions of rapidly exchanging conformations. Application to a 13-residue peptide with an 8-residue loop. *J. Am. Chem. Soc.* **1995**, *117*, 1027−1033.
(29) Nevins, N.; Cicero, D.; Snyder, J. P. A test of the single-conformation hypothesis in the analysis of NMR data for small polar molecules: A force field comparison. *J. Org. Chem.* **1999**, *64*, 3979−3986.
(30) Python.org. https://www.python.org/ (accessed July 16, 2014).
(31) CentOS Project. https://www.centos.org/ (accessed July 16, 2014).
(32) Atasoylu, O.; Smith, A. B. DISCON. http://discon.sourceforge.net/ (accessed July 16, 2014).
(33) Evans, D.; Sharman, G. Janocchio. http://janocchio.sourceforge.net/ (accessed July 16, 2014).
(34) Funaioli, T.; Cavazza, M.; Zandomeneghi, M.; Pietra, F. On the chiroptical behavior of conjugated multichromophoric compounds of a new pseudoaromatic class: Bicolchicides and biisocolchicides. *PLoS One* **2010**, *5*, e10617.
(35) Eguchi, T.; Kondo, K.; Kakinuma, K.; Uekusa, H.; Ohashi, Y.; Mizoue, K.; Qiao, Y.-F. Unique Solvent-Dependent Atropisomerism of a Novel Cytotoxic Naphthoxanthene Antibiotic FD-594. *J. Org. Chem.* **1999**, *64*, 5371−5376.
(36) Barroso, J. Transition State Search (QST2 & QST3) and IRC with Gaussian09. http://joaquinbarroso.com/2013/11/27/qst2-qst3/ (accessed July 16, 2014).
(37) Levy, G. C.; Lichter, R. L. *Nitrogen-15 Nuclear Magnetic Resonance Spectroscopy*; John Wiley & Sons: New York, 1979.
(38) Zartler, E.; Martin, G. The use of $^{1}H-^{31}P$ GHMBC and covariance NMR to unambiguously determine phosphate ester linkages in complex polysaccharide mixtures. *J. Biomol. NMR* **2011**, *51*, 357−367.
(39) Macchioni, A.; Pregosin, P. S.; Rüegger, H.; van Koten, G.; van der Schaaf, P. A.; Abbenhuis, R. A. T. M. ^{183}W NMR spectroscopy of W(VI) imidoaryl and imidoalkyl complexes using inverse detection based on non-specific long-range interactions. *Magn. Reson. Chem.* **1994**, *32*, 235−241.
(40) Biesemans, M.; Martins, J. C.; Willem, R.; Lyčka, A.; Růžička, A.; Holeček, J. $^{1}H,^{117}Sn$ *J*-HMBC spectroscopy as a tool for the determination of long-range ^{n}J ($^{1}H,^{117}Sn$) coupling constants in the investigation of intramolecular donor−acceptor interaction in [2-(*N,N*-dimethylaminomethyl)phenyl]stannanes. *Magn. Reson. Chem.* **2002**, *40*, 65−69.
(41) Biesemans, M.; Martins, J. C.; Jurkschat, K.; Pieper, N.; Seemeyer, S.; Willem, R. Assessing weak intramolecular donor−

acceptor interactions using ^{1}H-^{117}Sn *J*-HMQC spectroscopy. *Magn. Reson. Chem.* **2004**, *42*, 776−780.

(42) Gholivand, K.; Ghadimi, S.; Naderimanesh, H.; Forouzanfar, A. Dependence of the long-range phosphorus−hydrogen coupling constant ^{n}JP−H (n = 3,6,7) on the bond order between phosphorus and its substituents: Preparation and spectroscopic characterization of several phosphoramidates. *Magn. Reson. Chem.* **2001**, *39*, 684−688.

(43) Jones, C. R.; Butts, C. P.; Harvey, J. N. Accuracy in determining interproton distances using Nuclear Overhauser Effect data from a flexible molecule. *Beilstein J. Org. Chem.* **2011**, *7*, 145−150.

(44) Butts, C. P.; Jones, C. R.; Harvey, J. N. High precision NOEs as a probe for low level conformers-a second conformation of strychnine. *Chem. Commun.* **2011**, *47*, 1193−1195.

(45) Gaurrand, S.; Desjardins, S.; Meyer, C.; Bonnet, P.; Argoullon, J.-M.; Oulyadi, H.; Guillemont, J. Conformational analysis of R207910, a new drug candidate for the treatment of tuberculosis, by a combined NMR and molecular modeling approach. *Chem. Biol. Drug Des.* **2006**, *68*, 77−84.

(46) Nikiforovich, G. V.; Prakash, O.; Gehrig, C. A.; Hruby, V. J. Conformations of the dermenkephalin backbone in dimethyl sulfoxide solution by a new approach to the solution conformations of flexible peptides. *J. Am. Chem. Soc.* **1993**, *115*, 3399−3406.

(47) Chini, M. G.; Jones, C. R.; Zampella, A.; D'Auria, M. V.; Renga, B.; Fiorucci, S.; Butts, C. P.; Bifulco, G. Quantitative NMR-derived interproton distances combined with quantum mechanical calculations of ^{13}C chemical shifts in the stereochemical determination of conicasterol F, a nuclear receptor ligand from *Theonella swinhoei*. *J. Org. Chem.* **2011**, *77*, 1489−1496.

(48) Maeztu, R.; González-Gaitano, G.; Tardajos, G. Enhancement of the Chemiluminescence of two isoluminol derivatives by nano-encapsulation with natural cyclodextrins. *J. Phys. Chem. B* **2010**, *114*, 10541−10549.

(49) Ali, S. M.; Khan, S.; Crowyn, G. Structure determination of fexofenadine-α-cyclodextrin complex by quantitative 2D ROESY analysis and molecular mechanics studies. *Magn. Reson. Chem.* **2012**, *50*, 299−304.

(50) Mackeen, M.; Almond, A.; Cumpstey, I.; Enis, S. C.; Kupce, E.; Butters, T. D.; Fairbanks, A. J.; Dwek, R. A.; Wormald, M. R. The importance of including local correlation times in the calculation of inter-proton distances from NMR measurements: ignoring local correlation times leads to significant errors in the conformational analysis of the Glcα1−2Glcα linkage by NMR spectroscopy. *Org. Biomol. Chem.* **2006**, *4*, 2241−2246.

(51) Butts, C. P.; Jones, C. R.; Towers, E. C.; Flynn, J. L.; Appleby, L.; Barron, N. J. Interproton distance determinations by NOE − Surprising accuracy and precision in a rigid organic molecule. *Org. Biomol. Chem.* **2011**, *9*, 177−184.

(52) Borgias, B. A.; Gochin, M.; Kerwood, D. J.; James, T. L. Relaxation matrix analysis of 2D NMR data. *Prog. Nucl. Magn. Reson. Spectrosc.* **1990**, *22*, 83−100.

(53) Adamo, C.; Barone, V. Exchange functionals with improved long-range behavior and adiabatic connection methods without adjustable parameters: The mPW and mPW1PW models. *J. Chem. Phys.* **1998**, *108*, 664−675.

(54) Palermo, G.; Riccio, R.; Bifulco, G. Effect of electronegative substituents and angular dependence on the heteronuclear spin−spin coupling constant ^{3}JC−H: An empirical prediction equation derived by density functional theory calculations. *J. Org. Chem.* **2010**, *75*, 1982−1991.

(55) Ditchfield, R. Molecular orbital theory of magnetic shielding and magnetic susceptibility. *J. Chem. Phys.* **1972**, *56*, 5688−5691.

(56) Wolinski, K.; Hinton, J. F.; Pulay, P. Efficient implementation of the gauge-independent atomic orbital method for NMR chemical shift calculations. *J. Am. Chem. Soc.* **1990**, *112*, 8251−8260.

(57) Frisch, M. J.; Trucks, G. W.; Schlegel, H. B.; Scuseria, G. E.; Robb, M. A.; Cheeseman, J. R.; Scalmani, G.; Barone, V.; Mennucci, B.; Petersson, G. A.; Nakatsuji, H.; Caricato, M.; Li, X.; Hratchian, H. P.; Izmaylov, A. F.; Bloino, J.; Zheng, G.; Sonnenberg, J. L.; Hada, M.; Ehara, M.; Toyota, K.; Fukuda, R.; Hasegawa, J.; Ishida, M.; Nakajima, T.; Honda, Y.; Kitao, O.; Nakai, H.; Vreven, T.; Montgomery Jr., J. A.; Peralta, J. E.; Ogliaro, F.; Bearpark, M. J.; Heyd, J.; Brothers, E. N.; Kudin, K. N.; Staroverov, V. N.; Kobayashi, R.; Normand, J.; Raghavachari, K.; Rendell, A. P.; Burant, J. C.; Iyengar, S. S.; Tomasi, J.; Cossi, M.; Rega, N.; Millam, N. J.; Klene, M.; Knox, J. E.; Cross, J. B.; Bakken, V.; Adamo, C.; Jaramillo, J.; Gomperts, R.; Stratmann, R. E.; Yazyev, O.; Austin, A. J.; Cammi, R.; Pomelli, C.; Ochterski, J. W.; Martin, R. L.; Morokuma, K.; Zakrzewski, V. G.; Voth, G. A.; Salvador, P.; Dannenberg, J. J.; Dapprich, S.; Daniels, A. D.; Farkas, Ö.; Foresman, J. B.; Ortiz, J. V.; Cioslowski, J.; Fox, D. J. *Gaussian 09*; Gaussian, Inc.: Wallingford, CT, 2009.

(58) *MATLAB and Statistics Toolbox*, Release 2014a; The MathWorks, Inc., Natick, MA, 2014.

(59) Cox, B. D.; Prosser, A. R.; Katzman, B. M.; Alcaraz, A. A.; Liotta, D. C.; Wilson, L. J.; Snyder, J. P. Anti-HIV small-molecule binding in the peptide subpocket of the CXCR4:CVX15 crystal structure. *ChemBioChem.* **2014**, *15*, 1614−1620.

(60) Barboni, L.; Lambertucci, C.; Appendino, G.; Vander Velde, D. G.; Himes, R. H.; Bombardelli, E.; Wang, M.; Snyder, J. P. Synthesis and NMR-driven conformational analysis of taxol analogues conformationally constrained on the C13 side chain. *J. Med. Chem.* **2001**, *44*, 1576−1587.

(61) Metaferia, B. B.; Hoch, J.; Glass, T. E.; Bane, S. L.; Chatterjee, S. K.; Snyder, J. P.; Lakdawala, A.; Cornett, B.; Kingston, D. G. I. Synthesis and biological evaluation of novel macrocyclic paclitaxel analogues. *Org. Lett.* **2001**, *3*, 2461−2464.

(62) Ganesh, T.; Yang, C.; Norris, A.; Glass, T.; Bane, S.; Ravindra, R.; Banerjee, A.; Metaferia, B.; Thomas, S. L.; Giannakakou, P.; Alcaraz, A. A.; Lakdawala, A. S.; Snyder, J. P.; Kingston, D. G. I. Evaluation of the tubulin-bound paclitaxel conformation: Synthesis, biology, and SAR studies of C-4 to C-3′ bridged paclitaxel analogues. *J. Med. Chem.* **2007**, *50*, 713−725.